Science and Technology of Advanced Materials

ISSN: 1468-6996 (Print) 1878-5514 (Online) Journal homepage: www.tandfonline.com/journals/tsta20

Systematic investigation on transverse thermoelectric conversion of $RE_2(Fe,Co)_{14}B$ (RE = rare-earth) compounds

Babu Madavali, Fuyuki Ando, Takamasa Hirai, Andres Martin-Cid, Ken-ichi Uchida & Hossein Sepehri-Amin

To cite this article: Babu Madavali, Fuyuki Ando, Takamasa Hirai, Andres Martin-Cid, Ken-ichi Uchida & Hossein Sepehri-Amin (2025) Systematic investigation on transverse thermoelectric conversion of $RE_2(Fe,Co)_{14}B$ (RE = rare-earth) compounds, Science and Technology of Advanced Materials, 26:1, 2520162, DOI: 10.1080/14686996.2025.2520162

To link to this article: https://doi.org/10.1080/14686996.2025.2520162

SCIENCE AND TECHNOLOGY OF ADVANCED MATERIALS
2025, VOL. 26, NO. 1, 2520162
https://doi.org/10.1080/14686996.2025.2520162

Taylor & Francis
Taylor & Francis Group

FOCUS ISSUE ARTICLE

OPEN ACCESS Check for updates

Systematic investigation on transverse thermoelectric conversion of $RE_2(Fe,Co)_{14}B$ (RE = rare-earth) compounds

Babu Madavali[a*], Fuyuki Ando[a*], Takamasa Hirai[a], Andres Martin-Cid[a], Ken-ichi Uchida[a,b] and Hossein Sepehri-Amin[a]

[a]Research Center for Magnetic and Spintronic Materials, National Institute for Materials Science, Tsukuba, Japan;
[b]Department of Advanced Materials Science, Graduate School of Frontier Sciences, The University of Tokyo, Kashiwa, Japan

ABSTRACT

Transverse thermoelectric generation (TEG) based on the anomalous Nernst effect (ANE) is a promising technology capable of converting waste heat into electricity. The transverse TEG device can operate without applying an external magnetic field by implementing permanent magnets, such as $Nd_2Fe_{14}B$-type magnets. However, the transverse thermoelectric properties of the rare-earth (RE) based compounds have not been systematically studied and understood so far. In this work, we have explored the potential of $RE_2Fe_{14}B$ and $Nd_2(Fe, Co)_{14}B$ compounds and systematically investigated the transverse thermoelectric properties at room temperature. We obtained the negative anomalous Nernst coefficient (S_{ANE}) for all the $RE_2Fe_{14}B$ (RE = Tb, Dy, Ho, and Nd) alloys regardless of the RE element and the highest negative S_{ANE} of -0.67×10^{-6} VK^{-1} for $Tb_2Fe_{14}B$ among them, which is comparable to that of the commercial $Nd_2Fe_{14}B$ permanent magnets with an optimized microstructure. The substitution of Co for Fe site in $Nd_2(Fe_{1-p}Co_p)_{14}B$ alloys causes sign reversal (from negative to positive) of S_{ANE} values. The transverse thermoelectric conductivity is responsible for the sign change in S_{ANE} values. As a result, the $Nd_2(Fe_{0.4}Co_{0.6})_{14}B$ alloy shows the highest positive S_{ANE} of 1.87×10^{-6} VK^{-1}, revealing that the RE and 3*d* transition metal elements play distinct roles on the transverse thermoelectric performance in $RE_2(Fe,Co)_{14}B$ compounds.

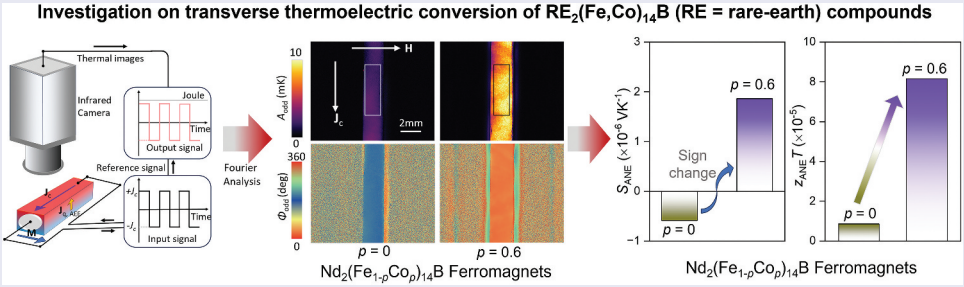

ARTICLE HISTORY
Received 15 December 2024
Accepted 11 June 2025
Revised 15 May 2025

KEYWORDS
Anomalous Nernst effect; permanent magnets; transverse thermoelectric conversion

IMPACT STATEMENT

This work systematically investigates rare-earth-based $RE_2Fe_{14}B$ compounds, uncovering tunable transverse thermoelectric properties, including anomalous Nernst coefficient sign reversal and a twofold enhancement via Co substitution, advancing efficient transverse thermoelectric generation technologies.

1. Introduction

Transverse thermoelectric generation (TEG) has garnered significant attention due to its ability to directly convert heat into electricity [1,2]. A typical TEG device based on the Seebeck effect consists of multiple *p*-type and *n*-type semiconductor legs, connected electrically in series and thermally in parallel using a large number of electrodes. However, such longitudinal TEG devices face unique challenges: thermal degradation at the hot side of the contacts, which significantly deteriorates the devices' output power, and performance degradation due to interfacial thermal and electrical resistances at many junctions [1,3,4]. In this context, transverse TEG devices offer key advantages over longitudinal TEG devices due to their simpler structures, which enables less junctions and

CONTACT Fuyuki Ando ANDO.Fuyuki@nims.go.jp; Hossein Sepehri-Amin H.SEPEHRIAMIN@nims.go.jp Research Center for Magnetic and Spintronic Materials, National Institute for Materials Science, Tsukuba 305-0047, Japan
*These authors contributed equally to this work.

Supplemental data for this article can be accessed online at https://doi.org/10.1080/14686996.2025.2520162

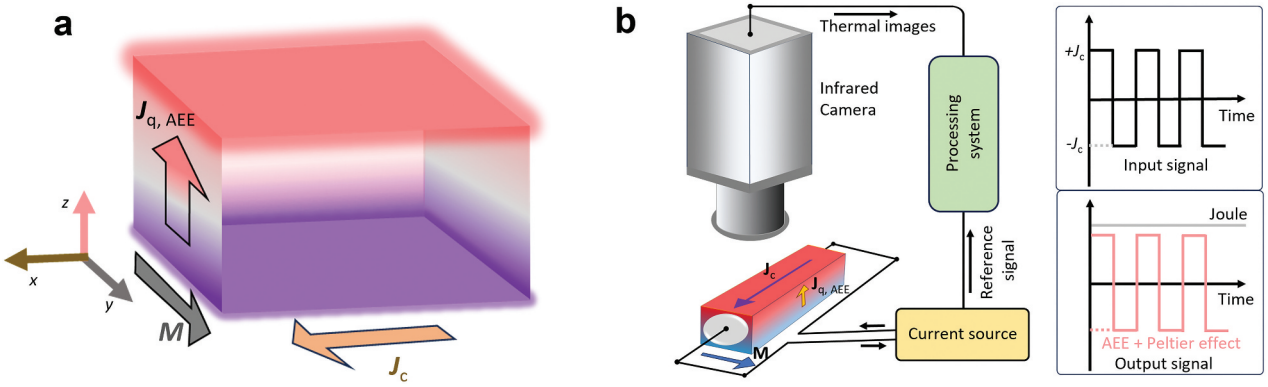

Figure 1. (a) Schematic of AEE in a ferromagnet in the in-plane magnetization configuration. $\mathbf{j}_{q,AEE}$, $\mathbf{j}_c$, and **M** denote the AEE-induced heat current, charge current applied to the ferromagnet, and magnetization vector. (b) Schematic of the LIT measurement set-up configurations. J_c denotes the square-wave amplitude of the charge current applied to the sample.

electrodes in modules. Consequently, these devices avoid the above degradations, significantly increasing efficiency closer to the theoretical limit than the conventional TEG devices [3–5].

In various transverse thermoelectric phenomena, the anomalous Nernst effect (ANE) has received much interest because of its simple lateral device structures and its intriguing physical mechanisms [6–18]. ANE refers to the generation of an electric field ($\mathbf{E}_{ANE}$) orthogonal to the magnetization direction and applied temperature gradient (T) in magnetic materials:

$$\mathbf{E}_{ANE} = S_{ANE}(\mathbf{m} \times \nabla T) \quad (1)$$

where **m** is a unit vector of the magnetization. The anomalous Ettingshausen effect (AEE) is the reciprocal to ANE in which the transverse heat current is generated in the direction orthogonal to the magnetization direction and applied charge current in magnetic materials, shown in Figure 1(a) [19–26]. The heat current density driven by AEE ($\mathbf{j}_{q,AEE}$) is defined as

$$\mathbf{j}_{q,AEE} = \Pi_{AEE}(\mathbf{j}_c \times \mathbf{m}) \quad (2)$$

where $\mathbf{j}_c$ and Π_{AEE} respectively denote the charge current density and anomalous Ettingshausen coefficient ($\Pi_{AEE} = S_{ANE}T$) [23,25–27]. Based on Equations 1 and 2, a finite spontaneous magnetization is required in materials for the manifestation of the ANE/AEE in transverse thermoelectric applications. Although elemental transition metals (e.g. Fe, Co) exhibit trivial ANE/AEE, recent development of spin caloritronics and topological materials science has revealed several magnetic alloys with large S_{ANE} and Π_{AEE} [6,7,11,15,16,27–30]. For example, Sakai et al. observed giant ANE in Co_2MnGa alloys with S_{ANE} ~6×10^{-6} VK^{-1} at room temperature by focusing on the Berry curvature of conduction electrons around Fermi energy [28]. Gautam et al. reported another strategy of enhancing ANE/AEE from the viewpoint of nanostructure engineering using iron-based amorphous alloys [30]. However, most of the ANE-based TEG devices using these materials require an external magnetic field (H) to align the magnetization direction.

To solve this problem, the use of permanent magnets with large remanent magnetization in ANE-based TEG devices is useful, enabling their thermoelectric operation without applying an external magnetic field [4,25,26]. Miura et al. investigated the transverse thermoelectric properties of different commercial sintered magnets and reported $SmCo_5$-type ($Nd_2Fe_{14}B$-type) permanent magnets under zero magnetic fields give the maximum S_{ANE} of 3.10×10^{-6} VK^{-1} (-0.76×10^{-6} VK^{-1}) at room temperature [25]. Recently, Ando et al. constructed a bulk TEG device consisting of these $SmCo_5$- and $Nd_2Fe_{14}B$-type permanent magnets and demonstrated the largest anomalous Nernst power density of 65 μWcm^{-2} under zero magnetic field [4]. However, the research so far on transverse thermoelectric properties of bulk permanent magnets has been focused on the commercially available magnets designed for the maximum energy product. Development of permanent magnets with excellent transverse thermoelectric properties requires fundamental research on their alloy and microstructure design.

In this work, we have systematically studied the transverse thermoelectric properties of $RE_2Fe_{14}B$-type compounds by changing the RE (RE = Tb, Dy, Ho, and Nd) elements. The f-electron system was chosen to make the compounds that exhibit strong magnetocrystalline anisotropy, particularly due to the RE – Fe exchange interactions and crystal electric field effects on the RE site [31]. This magnetic order affects charge carrier dynamics and thermal transport, which may favor the improvement in transverse thermoelectric properties. We found that all these compounds show negative S_{ANE} regardless of RE elements, and $Tb_2Fe_{14}B$ exhibits the largest S_{ANE} among them. In addition, we found that substitution

of Co for the Fe site in the $Nd_2Fe_{14}B$ system can change the sign of S_{ANE}; from negative in $Nd_2Fe_{14}B$ to positive in $Nd_2Co_{14}B$. At the intermediate composition for $Nd_2(Fe_{0.4}Co_{0.6})_{14}B$, the largest S_{ANE} of 1.87×10^{-6} VK^{-1} was observed. This study provides guidelines for the alloy design of permanent magnets for the development of transverse TEG devices.

2. Materials and methods

A series of $RE_2Fe_{14}B$ (RE = Tb, Dy, Ho, and Nd) and $Nd_2(Fe_{1-p}Co_p)_{14}B$ ($p = 0$, 0.2, 0.4, 0.6, 0.8, and 1.0) alloys were prepared by an induction melting process under an Ar atmosphere. The as-cast alloys were homogenized at 1150°C for 24 h in high vacuum conditions and quenched in water. The phase analysis of the ingots was evaluated by X-ray diffraction (XRD) (MiniFlex600, Rigaku) with Cr-Kα radiation. The XRD patterns were analyzed by the Rietveld method using the FullProf Suite [32]. Microstructural and chemical analyses were performed using a scanning electron microscope (SEM) (CrossBeam 1540 EsB, Carl Zeiss) equipped with an energy-dispersive X-ray spectroscopy (EDS) detector.

To investigate the transverse thermoelectric properties of $RE_2(Fe,Co)_{14}B$ alloys, we performed AEE using the lock-in thermography (LIT) technique using Enhanced Lock-In Thermal Emission (ELITE, DCG Systems G.K.) (Figure 1(b)) [23,25–27]. AEE measurements were conducted on rectangular-shaped samples (width and thickness of ~2–3 mm and a length of ~15 mm). The samples were placed on a plastic slab, which has a low thermal conductivity to reduce the heat loss due to thermal conduction. To enhance the infrared emissivity and ensure the homogenous emission properties, the top surface of the samples was coated with a black ink, the emissivity of which is >0.94 (JSC-3, JAPANSENSOR Corporation). The AEE measurements were conducted under the application of magnetic field, $\mu_0 H = 1$ T, with an atmospheric temperature and pressure. The thermal images were attained while applying a square-wave-modulated charge current with an amplitude J_c, frequency f, and zero offset to the sample along the x-direction and H along the y-direction. By extracting the first-harmonic component of the temperature modulation signal, the contributions of thermoelectric response, i.e. AEE and the Peltier effect, free from Joule heating, can be detected because Joule heating generated by such a charge current is constant over time [19,20,22,25]. The detected thermal images are transformed into the lock-in amplitude A and phase ϕ via Fourier analysis, where the A image gives the distribution of the magnitude of temperature modulation signals and the ϕ image shows the sign of the temperature modulation as well as the time delay due to thermal diffusion. By performing the LIT measurements under positive and negative H and evaluating the H-odd component of A and ϕ (A_{odd} and ϕ_{odd}, respectively), we can visualize the distribution of AEE-induced temperature modulation signals without the parasitic contribution by the Peltier effect [4,27,30]. In the present study, LIT measurements were performed at $\mu_0 H = \pm 1$ T. Since the present compounds are isotropic ferromagnetic ingots, it is necessary to accurately evaluate the magnetization at $\mu_0 H = 1$ T, M_{1T}, by taking into account the shape magnetic anisotropy. Therefore, we carefully determine M_{1T} using the same size Ni slab as a reference sample by vibrating sample magnetometry (VSM) and the same slabs used for the AEE measurement. The measurements of the anomalous Hall effect (AHE) were performed to estimate the transverse electrical resistivity ρ_{xy} using a physical property measurement system (PPMS, Quantum Design, Inc.). For this measurement, we applied H perpendicular to a DC charge current of 100 mA. The Seebeck coefficient S_{xx} and electrical conductivity σ of the samples were measured by Seebeck Coefficient/Electric Resistance Measurement System (ZEM-3, ADVANCE RIKO, Inc.). The thermal diffusivity measurements using the laser flash method and the specific heat measurements using the differential scanning calorimetry were performed to evaluate the thermal conductivity κ.

3. Results and discussion

3.1. Structural analysis of $RE_2Fe_{14}B$ alloys

The crystal structure and chemical composition analyses of $RE_2Fe_{14}B$ alloys are depicted in Figure 2. The XRD patterns were analyzed through Rietveld refinement, identifying the polycrystalline 2:14:1 phase as the main phase and indexed with (hkl) planes accordingly. The detailed Rietveld refinement analysis of all $RE_2Fe_{14}B$ alloys is shown in supplementary Figures S1–S4 and where several secondary phases were identified in addition to the main phase. The identified secondary phases include bcc-Fe, $NdFe_4B_4$, $TbFe_2$, $HoFe_3$, Ho_6Fe_{23}, and $DyFe_2$ and represent <10% in weight of the alloy phases [33,34]. The detailed microstructure characterization using SEM-EDS gives evidence that the samples are mainly made of 2:14:1 phase polycrystals as the matrix phase with homogeneously dispersed secondary phases (Figure 2(b)). The secondary phases identified by XRD can be

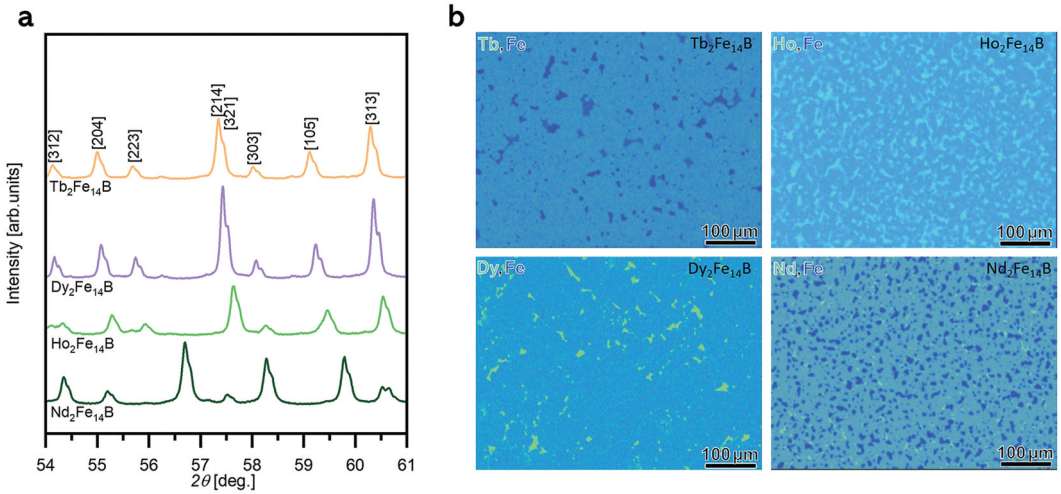

Figure 2. (a) Crystal structure analysis using XRD and (b) chemical composition analysis using SEM-EDS for the $RE_2Fe_{14}B$ alloys.

correlated to the different composition regions found in the SEM-EDS images, as examples are shown in supplementary Figures S1–S4. However, the identification of all secondary phases in the $Ho_2Fe_{14}B$ system remains challenging, and some of the secondary reflections found in XRD would not be identified with the existing phases.

3.2. Transverse thermoelectric properties of $RE_2Fe_{14}B$ alloys

Figure 3(a) represents the A_{odd} and ϕ_{odd} images at J_c = 1.0 A, $\mu_0 H = \pm 1$ T, and $f = 1$ hz for the $RE_2Fe_{14}B$ slabs. A clear current-induced temperature modulation was observed on the surface of the slabs due to the generation of $\mathbf{j}_{q,AEE}$ along the z direction through the x-directional input $\mathbf{j}_c$ and y--directional $\mathbf{m}$. Although the $Tb_2Fe_{14}B$, $Ho_2Fe_{14}B$, and $Nd_2Fe_{14}B$ slabs show the uniform distribution of the A_{odd} and ϕ_{odd} signals, the inhomogeneous distribution of the signals was observed in $Dy_2Fe_{14}B$, which can be explained by that only a part of magnetic domains reacts to the applied magnetic field due to the largest magnetocrystalline anisotropy among the $RE_2Fe_{14}B$ slabs (Figure 3(c)). Importantly, the sign of the AEE-induced temperature modulation on the surface for all the $RE_2Fe_{14}B$ slabs is negative (ϕ_{odd} ~180°), suggesting the negative sign of Π_{AEE} and S_{ANE} [25]. This result indicates that the substitution of the RE site has a minor influence on the sign of Π_{AEE} and S_{ANE} for $RE_2Fe_{14}B$. To estimate the S_{ANE} value from the results of the LIT measurements, we measured the f dependence of A_{odd} per unit charge current density j_c (i.e. A_{odd}/j_c) for $RE_2Fe_{14}B$. The A_{odd} value at each f was defined by averaging the A_{odd} values within the area defined by the rectangle of 1.2 × 3.9 mm^2 as indicated in Figure 3(a). As shown in Figure 3(b), the magnitude of A_{odd}/j_c gradually decreases with increasing f, which can be well reproduced by considering the thermal diffusion in the sample via the one-dimensional heat diffusion equation in the frequency domain (solid curves in Figure 3(b)) [25,27]. From the fitting curve in Figure 3(b), we estimated the A_{odd}/j_c value at the steady state, i.e. $f = 0$ hz, denoted as $A_{odd}{}^S/j_c$ at 1 T. The magnetization M curves of $RE_2Fe_{14}B$ were plotted in Figure 3(b). We found that M did not saturate at 1 T but increases up to 14 T (the maximum applied magnetic field in PPMS) (Figure 3(c)). Here, the M values at 14 T, M_{14T}, are regarded as the saturation magnetization M_s because they are comparable to the reported M_s in the literature (Supplementary Table S1) [35]. Π_{AEE} at the saturation state is thus estimated as [26]

$$\Pi_{AEE} = \frac{2\kappa A_{odd}^{S}}{j_c t} \cdot \frac{M_{14T}}{M_{1T}} \quad (3)$$

where t is the thickness in the z direction. Figure 4(a) shows the Π_{AEE} and S_{ANE} values for the $RE_2Fe_{14}B$ alloys. The calculated value of Π_{AEE} (S_{ANE}) for $Tb_2Fe_{14}B$ is -2.02×10^{-4} V (-0.67×10^{-6} VK^{-1}), which is the highest among them and comparable to the commercial $Nd_2Fe_{14}B$ permanent magnet [4,25]. It is noteworthy that the current $RE_2Fe_{14}B$ alloys do not have any microstructure control and texture, leaving room for further improvement of S_{ANE} through the nano- and/or microstructure engineering [30], as suggested by the difference in S_{ANE} between our $Nd_2Fe_{14}B$ and commercial $Nd_2Fe_{14}B$ slabs. Figure 4(b) shows the σ values, gradually increased from 0.42 to 1.10 × 10^6 Sm^{-1} by changing Tb to Nd in the $RE_2Fe_{14}B$ systems. These findings show a similar trend with the work of Stankiewicz et al. which showed that heavy RE such as $Tb_2Fe_{14}B$ systems

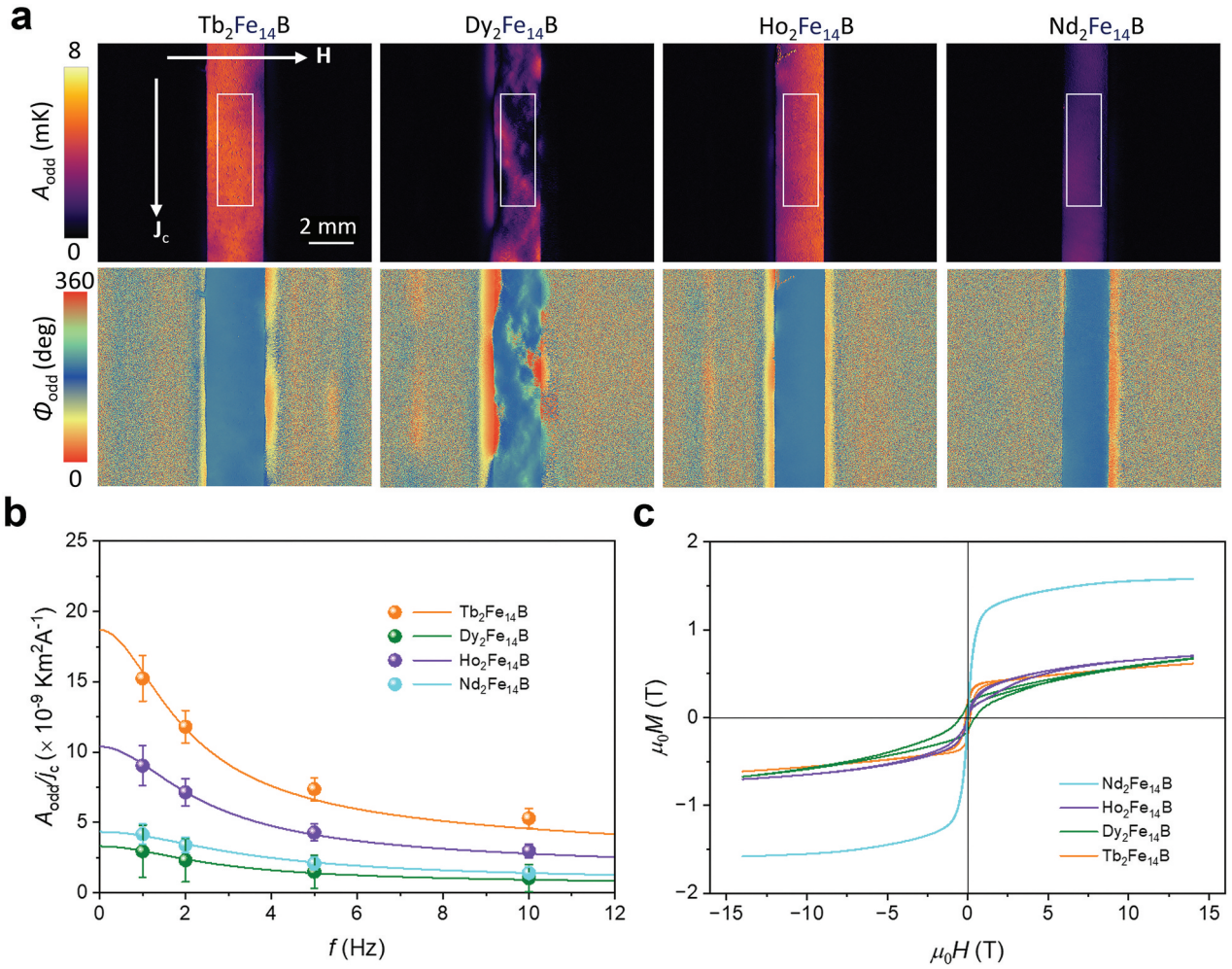

Figure 3. (a) A_{odd} and ϕ_{odd} images at $J_c = 1.0$ A, $\mu_0H = \pm 1$ T, and $f = 1$ Hz for the $RE_2Fe_{14}B$ (RE = Tb, Dy, Ho and Nd) alloys. (b) Frequency f dependence of A_{odd}/j_c. (c) Magnetic field H dependence of the magnetization M for the same $RE_2Fe_{14}B$ (RE = Tb, Dy, Ho and Nd) alloys.

exhibit lower electrical conductivity ($1/\rho_{xx}$) than $Nd_2Fe_{14}B$ system at ambient temperature [36]. Meanwhile, the commercial $Nd_2Fe_{14}B$-type permanent magnet shows 35% lower σ than the $Nd_2Fe_{14}B$ ingot. Since the commercial $Nd_2Fe_{14}B$ magnet had microstructural engineering, the charge carriers with low kinetic energies may get stopped by the presence of high density of grain boundaries, which leads to lower σ values compared to the ingots [37]. The κ values followed a similar trend to σ values in $RE_2Fe_{14}B$ systems, except for $Tb_2Fe_{14}B$ (Figure 4(c)). For a systematic understanding of κ, we estimated the electronic contribution κ_{el} and phonon contribution κ_{ph} of the thermal conductivity using $\kappa_{el} = \sigma LT$ and $\kappa_{ph} = \kappa - \kappa_{el}$, where L is the Lorenz number (2.44×10^{-8} $W\Omega K^{-2}$) and T is the absolute temperature (300 K) [2,30]. Not only κ_{el} but also κ_{ph} shows a similar trend to σ except for $Tb_2Fe_{14}B$ (Figure 4(d)). The uneven distribution of RE-rich phases (Figure 2(b)) may strongly scatter phonons at their interfaces with matrix, which is absent in the $Tb_2Fe_{14}B$, resulting in higher κ_{ph} [2]. Interestingly, the commercial $Nd_2Fe_{14}B$-type permanent magnet shows lower κ values than our $Nd_2Fe_{14}B$ ingot. The κ_{el} (κ_{ph}) is decreased from 8.31 (5.22) $Wm^{-1}K^{-1}$ to 5.42 (4.49) $Wm^{-1}K^{-1}$ for the commercial $Nd_2Fe_{14}B$-type permanent magnet. The κ_{el} is decreased due to their low σ values and κ_{ph} is decreased due to microstructural engineering and significant reduction in grain size compared to current ingots, which may induce the phonon scattering [37]. As a result, the obtained total κ values are lower than our ingot. Nevertheless, the intergranular phase particularly in the ultra-fine grain sized permanent magnets influences the thermal conductivity, as demonstrated by Kautsar et al. in the grain boundary engineered hot-deformed Nd-Fe-B magnets [38]

3.3. Evaluation of contribution factors for ANE in $RE_2Fe_{14}B$ alloys

The dominant contribution in ANE/AEE for our $RE_2Fe_{14}B$ systems is distinguished as follows. S_{ANE} can be divided into two components as [7,10,12–15,27,39]:

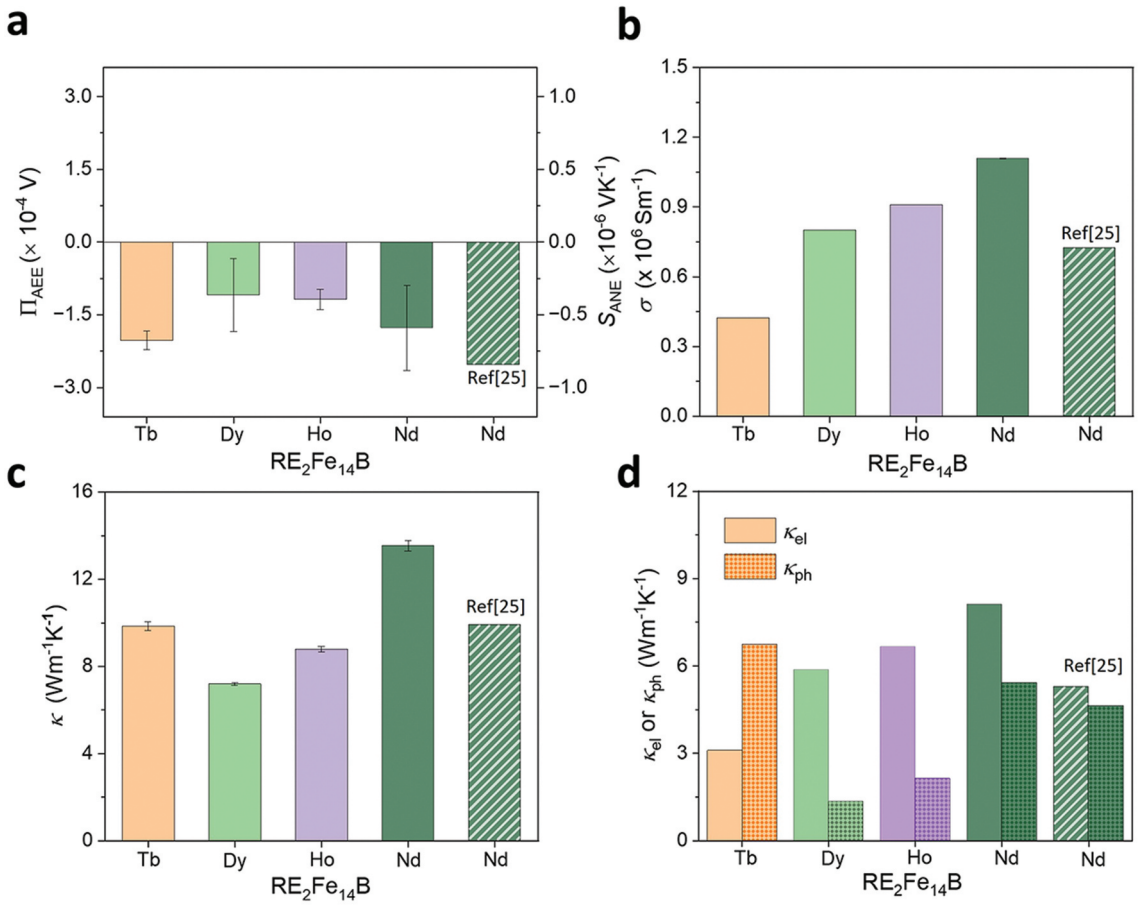

Figure 4. (a) $\Pi_{AEE}$and S_{ANE} ($= \Pi_{AEE}/T$), (b) σ, (c) κ, and (d) κ_{el} or κ_{ph} for the $RE_2Fe_{14}B$ (RE = Tb, Dy, Ho and Nd) alloys. The error bars represent the standard deviation of the measurements.

$$S_{ANE} = \rho_{xx}\alpha_{xy} + \rho_{xy}\alpha_{xx} = S_1 + S_2 \quad (4)$$

where $\rho_{xx} = 1/\sigma$ is the longitudinal resistivity and $\alpha_{xx}(\alpha_{xy})$ the diagonal component (off-diagonal component) of the thermoelectric conductivity tensor. S_1 originates from the transverse thermoelectric conductivity (α_{xy}) and S_2 is attributed to the synergistic action of the Seebeck effect and AHE. The S_2 term can be written as $S_2 = -S_{xx}\tan\theta_{AHE}$, where $S_{xx} = \rho_{xx}\alpha_{xx}$ and $\tan\theta_{AHE,} = -\rho_{xy}/\rho_{xx}$ with θ_{AHE} being the anomalous Hall angle [25,30]. We first evaluated $\tan\theta_{AHE}$ by measuring the H dependence of ρ_{xy} of the samples. Figure 5(a) shows ρ_{xy} as a function of H for the $RE_2Fe_{14}B$ samples. In the present work, we assumed that the contributions of the ordinary Nernst/Ettingshausen effect and the magnetic field dependence of the longitudinal transport properties are negligibly small in our samples. Using the ρ_{xy} values at $\mu_0 H = 14$ T, taken as the AHE contribution, we calculated the $\tan\theta_{AHE}$ values as shown in Figure 5(b). The $\tan\theta_{AHE}$ values are positive for all the $RE_2Fe_{14}B$ samples and $Dy_2Fe_{14}B$ shows the highest $\tan\theta_{AHE}$. Figure 5(c) represents S_{xx} for the $RE_2Fe_{14}B$ samples. The magnitude of S_{xx} is comparable for all the $RE_2Fe_{14}B$ samples. Figure 5(d) shows α_{xy}, estimated by substituting S_{ANE}, ρ_{xx}, S_{xx}, and $\tan\theta_{AHE}$ into Equation (4). The $RE_2Fe_{14}B$ samples show negative α_{xy} and $Nd_2Fe_{14}B$ shows the highest value among them. Furthermore, the S_1 and S_2 contributions to AEE/ANE are shown in Figure 5(e). S_{ANE} is determined by the compensation of the S_1 and S_2 contributions. It is clearly observed that the suppression of S_2 term while sustaining large negative S_1 term majorly decides the magnitude of the S_{ANE} values in the $RE_2Fe_{14}B$ samples.

3.4. Structural analysis of $Nd_2(Fe_{1-p}Co_p)_{14}B$ alloys

In this section, we did the same investigation on the substitution of the Fe site with Co in the $Nd_2(Fe_{1-p}Co_p)_{14}B$ alloys. The phase and purity of the $Nd_2(Fe_{1-p}Co_p)_{14}B$ ($p = 0$, 0.2, 0.4, 0.6, 0.8, and 1.0) homogenized alloys are depicted in Figure 6(a,b), respectively. XRD peak positions shift towards higher 2θ angles upon the Co substitution in Fe site in the $Nd_2(Fe_{1-p}Co_p)_{14}B$ ($p = 0$, 0.2, 0.4, 0.6, 0.8, and 1.0) alloys, evidencing a decrease in the lattice parameters. Rietveld refinement of the XRD patterns confirms the decrease in the lattice parameters a and c with the substitution

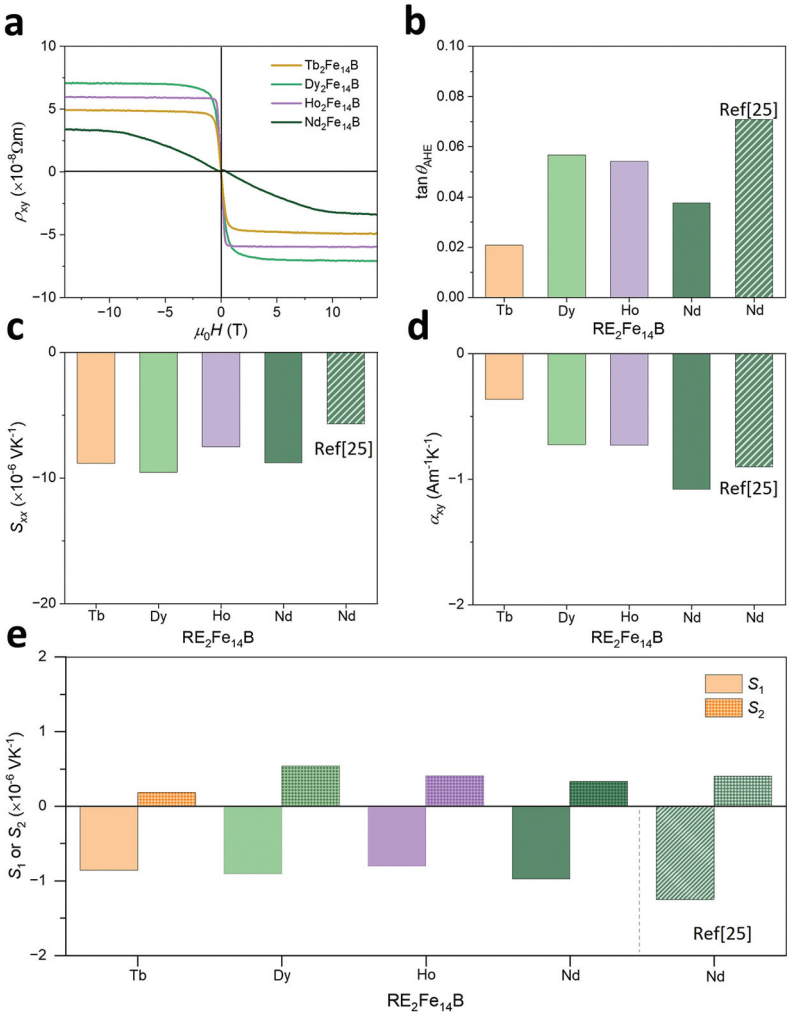

Figure 5. (a) ρ_{xy}, (b) tanθ_{AHE}, (c) S_{xx}, (d) α_{xy}, and (e) S_1 and S_2 for the $RE_2Fe_{14}B$ (RE = Tb, Dy, Ho and Nd) alloys.

of Fe for Co, by a total of 1.78% and 2.75%, respectively (see Table 1). This decrease in the lattice parameters is in agreement with the smaller atomic radius of Co compared to that of Fe, as well as previous literature [40]. The Rietveld refinement analysis of XRD (Supplementary Figures S5–S9) revealed that in addition to 2:14:1 matrix phase, some minor phases which often form as metallic or oxide phases in the 2:14:1 system including bcc-Fe, $NdCo_2$, $NdCo_4B$, and $NdCo_5$ exist in the homogenized $Nd_2(Fe_{1-p}Co_p)_{14}B$ alloys [41]. However, precise identification of the few secondary phases remains challenging, as they are present in a small volume fraction and might not be able to detectable in low-magnification SEM images, which provide more local information.

3.5. Transverse thermoelectric properties of $Nd_2(Fe_{1-x}Co_x)_{14}B$ alloys

The LIT technique was utilized to investigate AEE in the $Nd_2(Fe_{1-p}Co_p)_{14}B$ samples in the same manner as the previous experiments. The extracted A_{odd} and ϕ_{odd} images for $Nd_2(Fe_{1-p}Co_p)_{14}B$ are shown in Figure 7(a). The clear current-induced temperature modulation was obtained on the whole surface of the slabs. Although the ϕ_{odd} image of $Nd_2Fe_{14}B$ shows ~180°, the Co-substituted $Nd_2(Fe_{1-p}Co_p)_{14}B$ samples show a phase reversal to ~0° on the top surface [25,27,30]. The substitution of the transition metal in $Nd_2Fe_{14}B$ plays a significant role on the sign of Π_{AEE} and S_{ANE}. Figure 7(b) shows the f dependence of the A_{odd}/j_c values for the $Nd_2(Fe_{1-p}Co_p)_{14}B$ slabs, which are estimated by averaging the A_{odd} values within the area defined by the rectangle of 1.5 × 4.9 mm^2 as indicated in Figure 7(a). The Co-substituted $Nd_2(Fe_{1-p}Co_p)_{14}B$ samples show higher magnitude of A_{odd}/j_c than the pristine $Nd_2Fe_{14}B$ and $Nd_2(Fe_{0.4}Co_{0.6})_{14}B$ exhibits the highest A_{odd}^S/j_c value among them. The magnetization curves for the $Nd_2(Fe_{1-p}Co_p)_{14}B$ alloys are plotted in Figure 7(c).

Figure 8(a) shows the Π_{AEE} and S_{ANE} values for the $Nd_2(Fe_{1-p}Co_p)_{14}B$ alloys. The Π_{AEE} (S_{ANE}) value significantly improves more than twice in $Nd_2(Fe_{0.4}Co_{0.6})_{14}B$. Note that no strong correlation was found

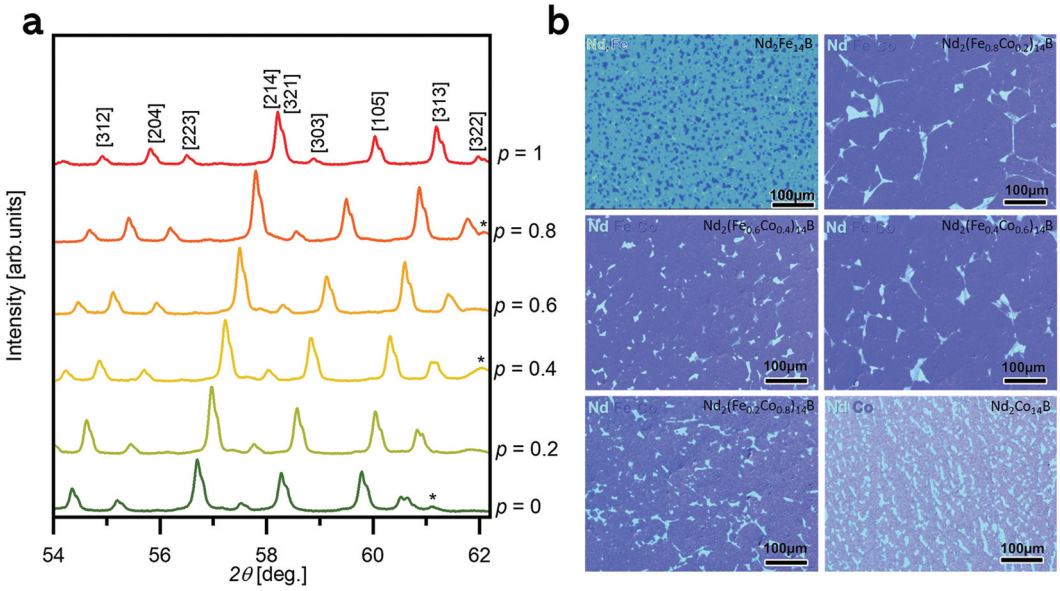

Figure 6. (a) Crystal structure analysis using XRD and (b) chemical composition analysis using SEM-EDS for the $Nd_2(Fe_{1-p}Co_p)_{14}B$ (p = 0, 0.2, 0.4, 0.6, 0.8, and 1.0) alloys.

Table 1. Lattice parameters for $Nd_2(Fe_{1-p}Co_p)_{14}B$ (p = 0, 0.2, 0.4, 0.6, 0.8, and 1) alloys.

$Nd_2(Fe_{1-p}Co_p)_{14}B$	a (Å)	c (Å)
p = 0	8.808	12.208
p = 0.2	8.786	12.162
p = 0.4	8.749	12.112
p = 0.6	8.711	12.051
p = 0.8	8.676	11.972
p = 1.0	8.651	11.872

between the S_{ANE} and M_s (Supplementary Figure S10) [5]. The σ and κ values are shown in Figure 8(b,c), respectively. The magnitude of the σ values exhibits a minimum for p = 0.4 in the $Nd_2(Fe_{1-p}Co_p)_{14}B$ alloys. Gu et al. reported that Fe d-orbital electrons primarily contribute to the total density of state (TDOS) at the Fermi level, with 2.31 states/eV atom in $Nd_2Fe_{14}B$.

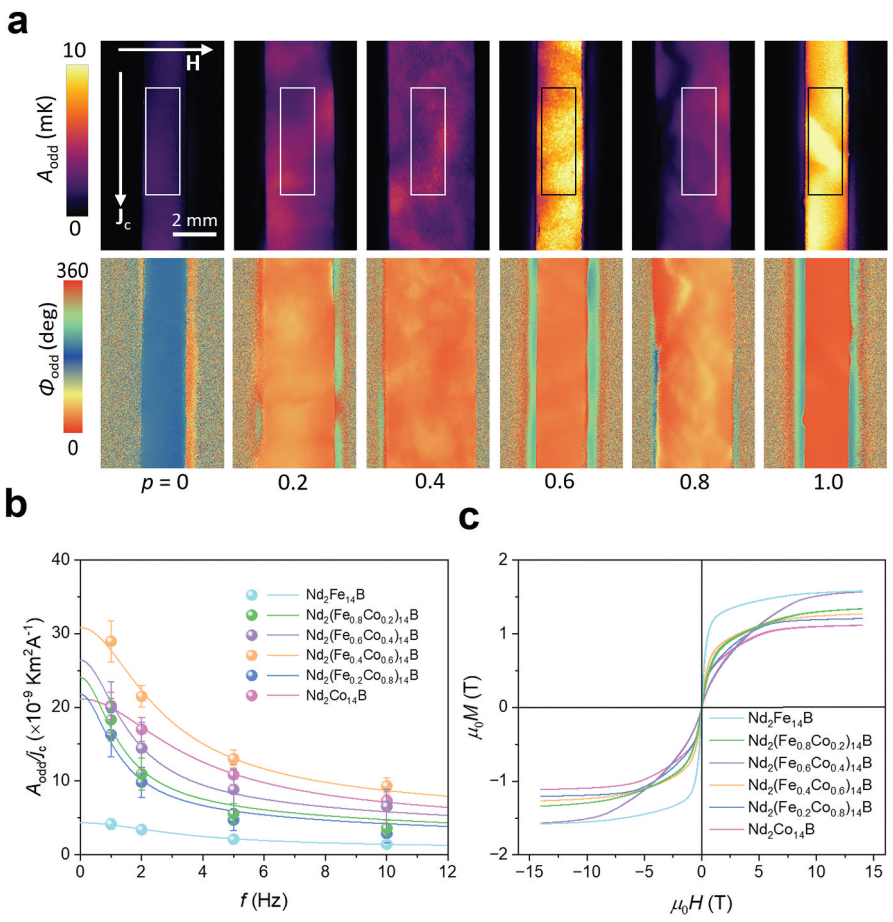

Figure 7. (a) A_{odd} and ϕ_{odd} images at J_c = 1.0 A, $\mu_0H = \pm$ 1 T, and f = 1 Hz for the $Nd_2(Fe_{1-p}Co_p)_{14}B$ (p = 0, 0.2, 0.4, 0.6, 0.8, and 1.0) alloys. (b) f dependence of A_{odd}/j_c. (c) H dependence of M for the same $Nd_2(Fe_{1-p}Co_p)_{14}B$ (p = 0, 0.2, 0.4, 0.6, 0.8, and 1.0) alloys.

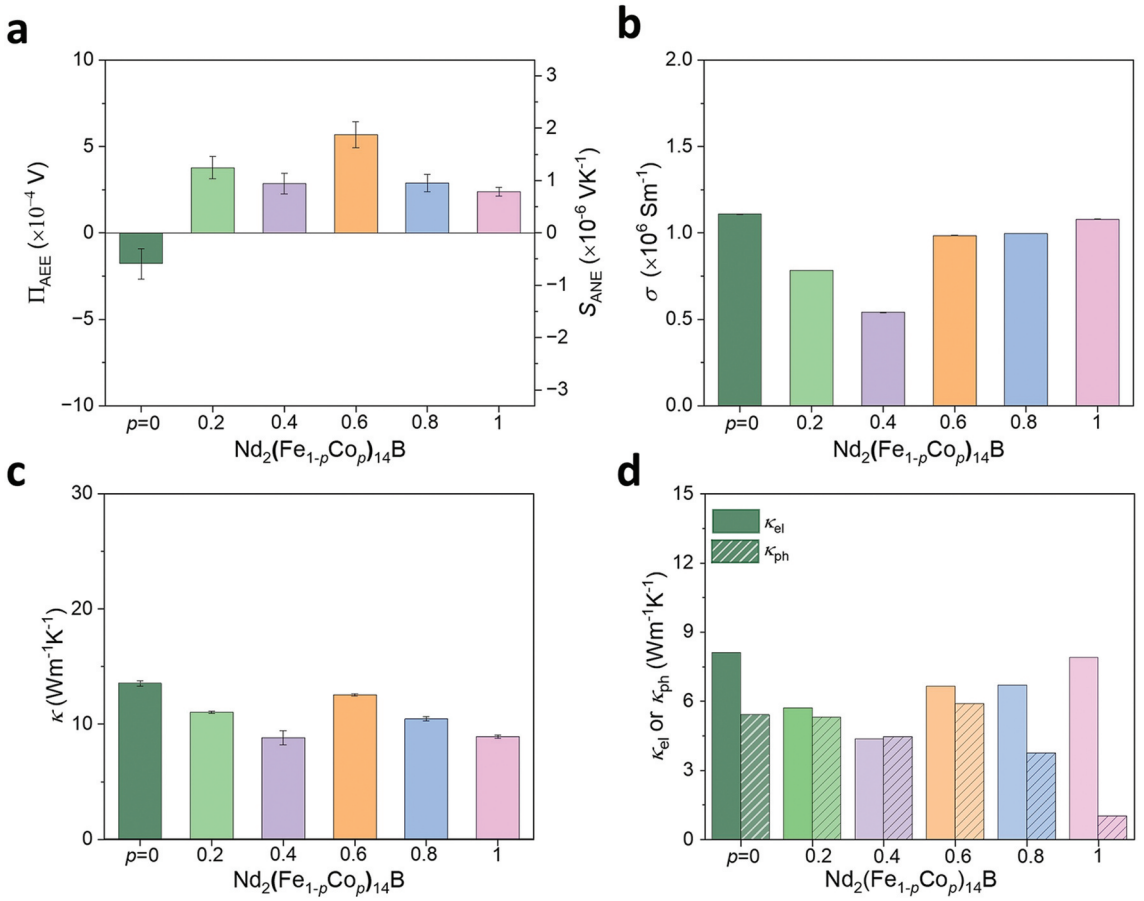

Figure 8. (a) $\Pi_{AEE}$and S_{ANE} (= Π_{AEE}/T), (b) σ, (c) κ, and (d) κ_{el} or κ_{ph} for the $Nd_2(Fe_{1-p}Co_p)_{14}B$ (p = 0, 0.2, 0.4, 0.6, 0.8, and 1.0) alloys. The error bars represent the standard deviation of the measurements.

This value is decreased to 2.06 states/eV atom when Co replaced for Fe, where the Co *d*-orbital electrons become responsible for the TDOS at Fermi level in Nd₂Co₁₄B [42,43]. By assuming the rigid band model, the decrease in σ observed in the present work can be attributed to the slight reduction in TDOS at the Fermi level due to domination of the Co *d*-orbital electrons in the $Nd_2(Fe_{1-p}Co_p)_{14}B$ system. On the other hand, the κ values are slightly decreased for the Co-substituted $Nd_2(Fe_{1-p}Co_p)_{14}B$ alloys, and the values are spread in the 9–12 $Wm^{-1}K^{-1}$ range. The $\kappa_{el}$and κ_{ph} contributions to the total κ are shown in Figure 8(d). The κ_{ph} has similar values but is significantly reduced for $Nd_2Co_{14}B$. The alloys with $p \geq 0.8$ have a higher density of Nd-rich phases (Figure 6(b)) compared to the others, which may scatter the phonons at their interfaces with matrix, leading to a decrease in κ_{ph}[2].

3.6. Evaluation of contribution factors for ANE in $Nd_2(Fe_{1-p}Co_p)_{14}B$ alloys

To elucidate the contribution factors for transverse thermoelectric properties in the $Nd_2(Fe_{1-p}Co_p)_{14}B$ alloys, we estimated S_1 and S_2. The H dependence of ρ_{xy} for the $Nd_2(Fe_{1-p}Co_p)_{14}B$ alloys is shown in Figure 9(a). The ρ_{xy} values at $\mu_0 H = 14$ T are taken as the AHE contribution. By using the ρ_{xy} values, $\tan\theta_{AHE}$ is evaluated and shown in Figure 9(b). The estimated $\tan\theta_{AHE}$ values are positive for all the $Nd_2(Fe_{1-p}Co_p)_{14}B$ samples, and $Nd_2Co_{14}B$ shows the smallest magnitude among them. The S_{xx} values for all the ingots are shown in Figure 9(c) and all of them exhibit negative sign. The magnitude of S_{xx} is comparable for all samples except for $Nd_2Co_{14}B$. Using the obtained S_{ANE}, S_{xx}, and $\tan\theta_{AHE}$ values, α_{xy} is estimated and shown in Figure 9(d). It is found that, although the pristine $Nd_2Fe_{14}B$ exhibits negative sign of α_{xy}, the Co-substituted $Nd_2(Fe_{1-p}Co_p)_{14}B$ samples display positive sign. This change might be due to the modification of the TDOS at the Fermi level, primarily caused by the change in the lattice parameter and contribution of Co *d*-orbital electrons in the Co-rich $Nd_2Fe_{14}B$ alloys [42,43]. Notably, the sign of α_{xy} is prominently responsible for the sign changes in the S_{ANE} values of $Nd_2(Fe_{1-p}Co_p)_{14}B$. The obtained S_1 and S_2 values are positive for the Co-substituted $Nd_2(Fe_{1-p}Co_p)_{14}B$ (Figure 9(e)). Based on the outcomes, it is argued that the S_1 and S_2 values constructively contribute to the total S_{ANE}.

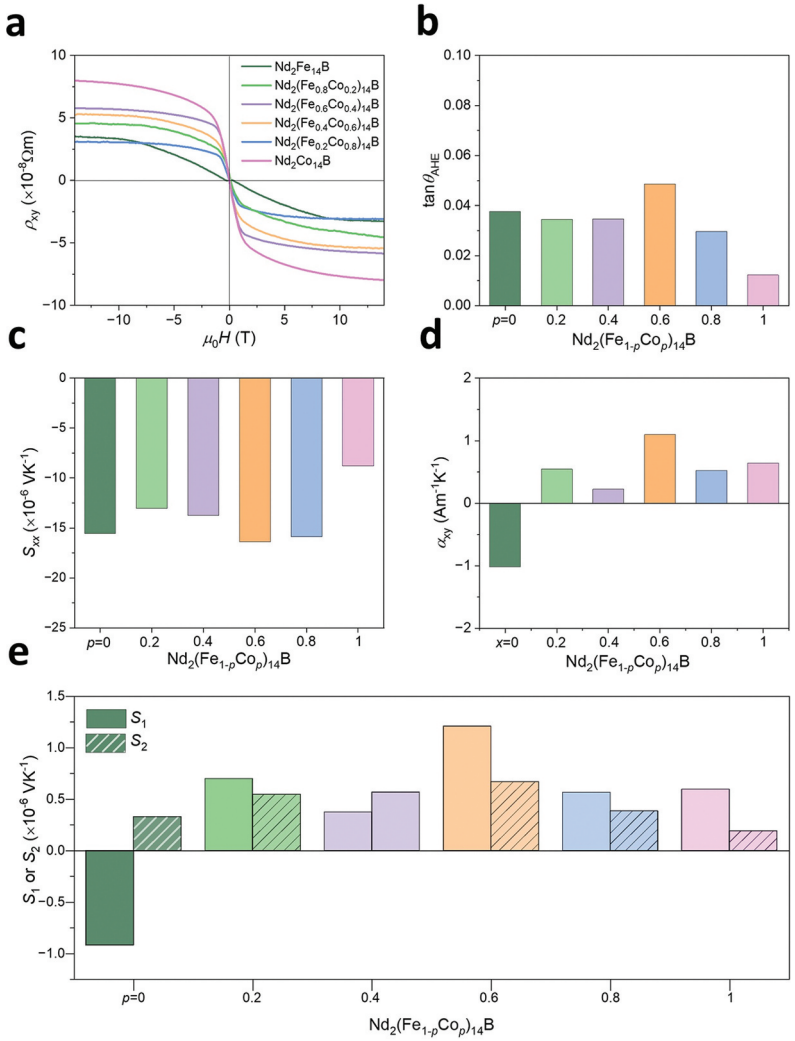

Figure 9. (a) ρ_{xy}, (b) $\tan\theta_{AHE}$, (c) S_{xx}, (d) α_{xy}, and (e) S_1 and S_2 for the $Nd_2(Fe_{1-p}Co_p)_{14}B$ ($p = 0$, 0.2, 0.4, 0.6, 0.8, and 1.0) alloys.

Finally, we quantitatively compared the S_{ANE} and dimensionless figure of merit $z_{ANE}T$ values for the commercial $Nd_2Fe_{14}B$ permanent magnet in the literature with our alloys (Figure 10(a,b)). $z_{ANE}T$ for transverse thermoelectric conversion due to ANE is estimated by the following expression [25–27,30]:

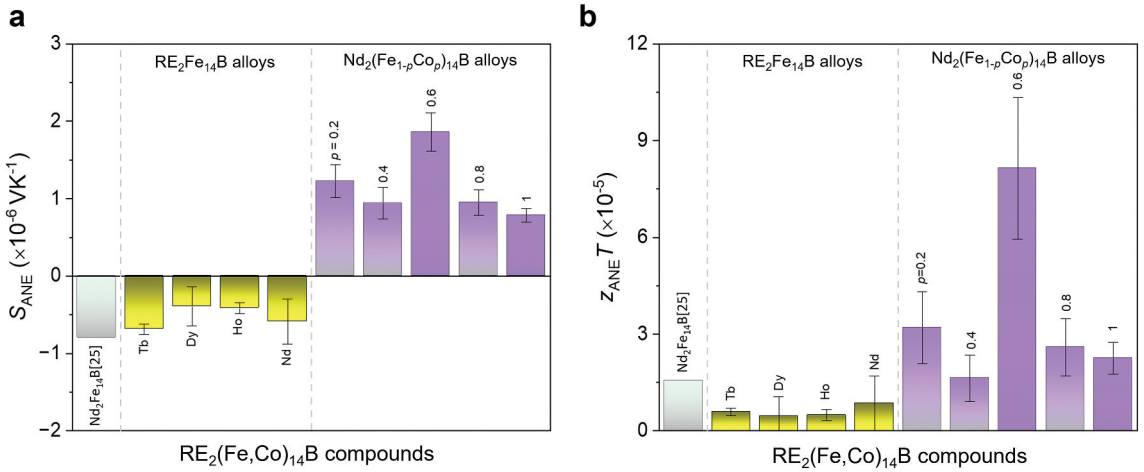

Figure 10. Comparison of (a) S_{ANE} and (b) $z_{ANE}T$ for commercial $Nd_2Fe_{14}B$ permanent magnets with those for our alloys measured at room temperature. The error bars represent the standard deviation of the measurements.

$$z_{\mathrm{ANE}}T = \frac{\Pi_{\mathrm{AEE}}^2 \sigma}{\kappa}\frac{1}{T} = \frac{S_{\mathrm{ANE}}^2 \sigma}{\kappa}T \quad (5)$$

Using the measured S_{ANE}, σ and κ values, $z_{\mathrm{ANE}}T$ is estimated using Equation (5). Importantly, the $Tb_2Fe_{14}B$ and $Nd_2Fe_{14}B$ alloys show almost similar negative S_{ANE}, but lower $z_{\mathrm{ANE}}T$ than the commercial $Nd_2Fe_{14}B$ magnet due to higher κ values. In turn, the $Nd_2(Fe_{1-p}Co_p)_{14}B$ alloys show the sign change and significant improvement in S_{ANE} as well as $z_{\mathrm{ANE}}T$. The largest estimated $z_{\mathrm{ANE}}T$ of 8.29×10^{-5} is obtained for the $Nd_2(Fe_{0.4}Co_{0.6})_{14}B$ composition due to their higher S_{ANE}. We found that $z_{\mathrm{ANE}}T$ in the $Nd_2(Fe_{0.4}Co_{0.6})_{14}B$ alloys is more than nine folds higher than that of the pristine $Nd_2Fe_{14}B$ alloy. These results highlight the importance of fundamental research to improve the transverse thermoelectric properties of compounds with large magnetocrystalline anisotropy. Such studies will guide material selection for the development of permanent magnets with optimized micro/nanostructures for transverse thermoelectric generation devices with improved anomalous Nernst power density.

4. Conclusions

We systematically investigated ANE/AEE in RE-based alloys with large magnetocrystalline anisotropy for ANE-based TEG devices operating without an external magnetic field. We observed that all $RE_2Fe_{14}B$ alloys exhibit negative S_{ANE} due to the negative sign of the transverse thermoelectric conductivity α_{xy} regardless of the RE element. Among them, $Tb_2Fe_{14}B$ compound shows the largest negative S_{ANE}, comparable to that of the commercially available $Nd_2Fe_{14}B$-type permanent magnet. Our work also confirmed that substituting Co for Fe site in the $Nd_2(Fe_{1-p}Co_p)_{14}B$ compounds alters the sign of S_{ANE}. A more than twofold improvement in the magnitude of S_{ANE} was obtained in the $Nd_2(Fe_{0.4}Co_{0.6})_{14}B$ alloy compared with the pristine $Nd_2Fe_{14}B$. Both S_1 and S_2 contributions constructively increase S_{ANE} in the $Nd_2(Fe_{1-p}Co_p)_{14}B$ compounds. The S_{ANE} values of the developed RE-TM-B alloys are comparable to those of existing commercial permanent magnets. This result suggests a significant potential for further enhancement of S_{ANE} by controlling microstructures and processing parameters, paving the way for sustainable energy applications using ANE-based TEG devices.

Acknowledgments

The authors thank H. Sebata and N. Kurata for technical support.

Disclosure statement

No potential conflict of interest was reported by the author(s).

Funding

This work was supported by ERATO "Magnetic Thermal Management Materials" [Grant No. JPMJER2201] from Japan Science and Technology Agency (JST) and Grants-in-Aid for Scientific Research (KAKENHI) [No. 24K17610] from Japan Society for the Promotion of Science (JSPS).

ORCID

Babu Madavali http://orcid.org/0000-0002-8486-701X
Fuyuki Ando http://orcid.org/0009-0003-7789-8170
Takamasa Hirai http://orcid.org/0000-0002-5577-8018
Andres Martin-Cid http://orcid.org/0000-0002-9711-288X
Ken-ichi Uchida http://orcid.org/0000-0001-7680-3051
Hossein Sepehri-Amin http://orcid.org/0000-0002-7856-7897

References

[1] Min G, Rowe DM. Optimisation of thermoelectric module geometry for waste heat electric power generation. J Power Sources. 1992;38(3):253–259. doi: 10.1016/0378-7753(92)80114-Q
[2] Snyder GJ, Toberer ES. Complex thermoelectric materials. Nat Mater. 2008;7(2):105–114. doi: 10.1038/nmat2090
[3] Uchida K, Heremans JP. Thermoelectrics: from longitudinal to transverse. Joule. 2022;6(10):2240–2245. doi: 10.1016/j.joule.2022.08.016
[4] Ando F, Hirai T, Uchida K. Permanent-magnet-based transverse thermoelectric generator with high fill factor driven by anomalous Nernst effect. APL Energy. 2024;2(1):016103. doi: 10.1063/5.0180506
[5] Uchida K, Zhou W, Sakuraba Y. Transverse thermoelectric generation using magnetic materials. Appl Phys Lett. 2021;118(14):140504. doi: 10.1063/5.0046877
[6] Sakai A, Minami S, Koretsune T, et al. Iron-based binary ferromagnets for transverse thermoelectric conversion. Nature. 2020;581(7806):53–57. doi: 10.1038/s41586-020-2230-z
[7] Sakuraba Y, Hyodo K, Sakuma A, et al. Giant anomalous Nernst effect in the $Co_2MnAl_{1-x}Si_x$ heusler alloy induced by Fermi level tuning and atomic ordering. Phys Rev B. 2020;101(13):134407. doi: 10.1103/PhysRevB.101.134407
[8] Mizuguchi M, Ohata S, Uchida K, et al. Anomalous Nernst effect in an $L1_0$-ordered epitaxial FePt thin film. Appl Phys Express. 2012;5(9):093002. doi: 10.1143/APEX.5.093002
[9] Hasegawa K, Mizuguchi M, Sakuraba Y, et al. Material dependence of anomalous Nernst effect in perpendicularly magnetized ordered-alloy thin films. Appl Phys Lett. 2015;106(25):252405. doi: 10.1063/1.4922901
[10] Sakuraba Y, Hasegawa K, Mizuguchi M, et al. Anomalous Nernst effect in $L1_0$-FePt/MnGa thermopiles for new thermoelectric applications. Appl Phys

Express. 2013;6(3):033003. doi: 10.7567/APEX.6.033003
[11] Nakayama H, Masuda K, Wang J, et al. Mechanism of strong enhancement of anomalous Nernst effect in Fe by Ga substitution. Phys Rev Mater. 2019;3(11):114412. doi: 10.1103/PhysRevMaterials.3.114412
[12] Uchida K, Kikkawa T, Seki T, et al. Enhancement of anomalous Nernst effects in metallic multilayers free from proximity-induced magnetism. Phys Rev B. 2015;92(9):094414. doi: 10.1103/PhysRevB.92.094414
[13] Zhou W, Sakuraba Y. Heat flux sensing by anomalous Nernst effect in Fe-Al thin films on a flexible substrate. Appl Phys Express. 2020;13(4):043001. doi: 10.35848/1882-0786/ab79fe
[14] Yamauchi T, Hamada Y, Kurokawa Y, et al. Anomalous Nernst effect dependence on composition in $Fe_{100-X}Rh_X$ alloys. Jpn J Appl Phys. 2022;61(SC):SC1019. doi: 10.35848/1347-4065/ac3ef1
[15] Ikhlas M, Tomita T, Koretsune T, et al. Large anomalous Nernst effect at room temperature in a chiral antiferromagnet. Nat Phys. 2017;13(11):1085–1090. doi: 10.1038/nphys4181
[16] Guin SN, Manna K, Noky J, et al. Anomalous Nernst effect beyond the magnetization scaling relation in the ferromagnetic heusler compound Co_2MnGa. NPG Asia Mater. 2019;11(1):16. doi: 10.1038/s41427-019-0116-z
[17] Miyasato T, Abe N, Fujii T, et al. Crossover behavior of the anomalous hall effect and anomalous Nernst effect in itinerant ferromagnets. Phys Rev Lett. 2007;99(8):086602. doi: 10.1103/PhysRevLett.99.086602
[18] Hirai T, Ando F, Sepehri-Amin H, et al. Hybridizing anomalous Nernst effect in artificially tilted multilayer based on magnetic topological material. Nat Commun. 2024;15(1):9643. doi: 10.1038/s41467-024-53723-2
[19] Das R, Iguchi R, Uchida K. Systematic investigation of anisotropic magneto-Peltier effect and anomalous Ettingshausen effect in Ni thin films. Phys Rev Appl. 2019;11(3):034022. doi: 10.1103/PhysRevApplied.11.034022
[20] Seki T, Iguchi R, Takanashi K, et al. Visualization of anomalous Ettingshausen effect in a ferromagnetic film: direct evidence of different symmetry from spin Peltier effect. Appl Phys Lett. 2018;112(15):152403. doi: 10.1063/1.5022759
[21] Modak R, Uchida K. Enhancement of temperature change induced by anomalous Ettingshausen effect in thin Ni films on suspended membrane substrates. Appl Phys Lett. 2020;116(3):032403. doi: 10.1063/1.5139976
[22] Seki T, Iguchi R, Takanashi K, et al. Relationship between anomalous Ettingshausen effect and anomalous Nernst effect in an FePt thin film. J Phys D. 2018;51(25):254001. doi: 10.1088/1361-6463/aac481
[23] Seki T, Miura A, Uchida K, et al. Anomalous Ettingshausen effect in ferrimagnetic Co-Gd. Appl Phys Express. 2019;12(2):023006. doi: 10.7567/1882-0786/aafb5a
[24] Bridgman PW. The connections between the four transverse galvanomagnetic and thermomagnetic phenomena. Phys Rev. 1924;24(6):644–651. doi: 10.1103/PhysRev.24.644
[25] Miura A, Sepehri-Amin H, Masuda K, et al. Observation of anomalous Ettingshausen effect and large transverse thermoelectric conductivity in permanent magnets. Appl Phys Lett. 2019;115(22):222403. doi: 10.1063/1.5131001
[26] Miura A, Masuda K, Hirai T, et al. High-temperature dependence of anomalous Ettingshausen effect in SmCo5-type permanent magnets. Appl Phys Lett. 2020;117(8):082408. doi: 10.1063/5.0023111
[27] Nagasawa R, Oyanagi K, Hirai T, et al. Anomalous Ettingshausen effect in iron-carbon alloys. Appl Phys Lett. 2022;121(6):062401. doi: 10.1063/5.0103248
[28] Sakai A, Mizuta YP, Nugroho AA, et al. Giant anomalous Nernst effect and quantum-critical scaling in a ferromagnetic semimetal. Nat Phys. 2018;14(11):1119–1124. doi: 10.1038/s41567-018-0225-6
[29] Wuttke C, Caglieris F, Sykora S, et al. Berry curvature unravelled by the anomalous Nernst effect in Mn3 Ge. Phys Rev B. 2019;100(8):085111. doi: 10.1103/PhysRevB.100.085111
[30] Gautam R, Hirai T, Alasli A, et al. Creation of flexible spin-caloritronic material with giant transverse thermoelectric conversion by nanostructure engineering. Nat Commun. 2024;15(1):2184. doi: 10.1038/s41467-024-46475-6
[31] Coey JMD. Rare-earth iron permanent magnets. Oxford (England): Oxford University Press; 1996. doi: 10.1093/oso/9780198517924.001.0001
[32] Rodriguez-Carvajal J. Recent advances in magnetic structure determination neutron powder diffraction. Physica-B. 1993;192(1–2):55–69. doi: 10.1016/0921-4526(93)90108-I
[33] Koylu-Alkan O, Barandiaran JM, Salazar D, et al. Submicron $R_2Fe_{14}B$ particles. AIP Adv. 2016;6(5):056027. doi: 10.1063/1.4944771
[34] Martín VEM. Relaciones entre la microestructura y las propiedades histereticas en el sistema Nd-Dy-Fe-B [dissertation]. Madrid: Universidad Complutense de madrid; 2002.
[35] Sagawa M, Fujimura S, Yamamoto H, et al. Permanent magnet materials based on the rare earth-iron-boron tetragonal compounds. IEEE Trans Magn. 1984;20(5):1584–1589. doi: 10.1109/TMAG.1984.1063214
[36] Stankiewicz J, Bartolomé J, Hirosawa S. Magnetotransport properties through phase transitions in $R_2Fe_{14}B$(R=Y,Nd,Tm) compounds. Phys Rev B Condens Matter Mater Phys. 2001;64(9):094428. doi: 10.1103/PhysRevB.64.094428
[37] Hu C, Xia K, Fu C, et al. Carrier grain boundary scattering in thermoelectric materials. Energy Environ Sci. 2022;15(4):1406–1422. doi: 10.1039/d1ee03802h
[38] Kautsar ZH, Madavali B, Hirai T, et al. Impact of intergranular phase variations on the anomalous Nernst effect in Nd-Fe-B permanent magnets. Energy Mater. 2025:5. doi: 10.20517/energymater.2025.26
[39] Modak R, Zhou W, Sakuraba Y, et al. Comparison of the in-plane coercive field and anomalous Nernst effect between a co-sputtered Sm-Co amorphous film and Sm/Co multilayer amorphous films with various layer thicknesses. Appl Phys Express. 2023;16(5):053003. doi: 10.35848/1882-0786/acd103
[40] Herbst JF, Yelon WB. Preferential site occupation and magnetic structure of $Nd_2(Co_xFe_{1-x})_{14}B$ systems. J Appl Phys. 1986;60(12):4224–4229. doi: 10.1063/1.337511

[41] Fuerst CD, Herbst JF. Hard magnetic properties of melt-spun Nd-Co-Fe-B materials. J Appl Phys. 1988;63(8):3324–3326. doi: 10.1063/1.340825
[42] Gu Z-Q, Ching WY. Comparative studies of electronic and magnetic structures. Phys Rev B. 1987;36 (16):8530–8546. doi: 10.1103/PhysRevB.36.8530
[43] Yu J, Jiang S, Sun D, et al. Correlation of Mechanical properties and electronic structures for NdFeB permanent magnet under hydrostatic pressure based on first-principle calculation. J Mater Res Technol. 2022;18:3410–3427. doi: 10.1016/j.jmrt.2022.03.189